Nano Research
2022, 15(9): 7925–7932

ISSN 1998-0124 CN 11-5974/O4
https://doi.org/10.1007/s12274-022-4453-9

Research Article

Quantitative defect regulation of heterostructures for sulfur catalysis toward fast and long lifespan lithium-sulfur batteries

Saisai Qiu[1,§], Xinqi Liang[1,§], Shuwen Niu[2], Qingguo Chen[1], Gongming Wang[2] (✉), and Minghua Chen[1] (✉)

[1] *Key Laboratory of Engineering Dielectric and Applications (Ministry of Education), School of Electrical and Electronic Engineering, Harbin University of Science and Technology, Harbin 150080, China*
[2] *Hefei National Laboratory for Physical Science at the Microscale, Department of Chemistry, University of Science & Technology of China, Hefei 230026, China*
[§] *Saisai Qiu and Xinqi Liang contributed equally to this work.*

Received: 7 March 2022 / **Revised:** 28 March 2022 / **Accepted:** 20 April 2022

ABSTRACT

The advancement of lithium-sulfur (Li-S) batteries is severely retarded by lithium polysulfides (LiPSs) shuttling behavior and sluggish redox kinetics. Herein, the heterogeneous composite with defective Bi_2Se_{3-x} nanosheets and porous nitrogen-doped carbon (Bi_2Se_{3-x}/NC) is prepared by selenizing bismuth metal-organic frameworks as a multifunctional sulfur host. The highly efficient immobilization-conversion on LiPSs is realized by the synergistic effect of structure construction strategy and defect engineering. It is found that Bi_2Se_{3-x} with the suitable amount of selenium vacancies achieves the best electrochemical performance due to the advantages of its structure and composition. These results confirm the intrinsic correlation between defects and catalysis, which are revealed by computational and experimental studies. Due to these superiorities, the developed sulfur electrodes exhibited admirable stability and a fairly lower capacity decay rate of approximately 0.0278% per cycle over 1,000 cycles at a 3 C rate. Even at the high sulfur loading of 6.2 mg·cm^{-2}, the cathode still demonstrates a high discharge capacity of 455 mAh·g^{-1} at 1 C. This work may enlighten the development of mechanism investigation and design principles regarding sulfur catalysis toward high-performance Li-S batteries.

KEYWORDS

lithium-sulfur (Li-S) batteries, lithium polysulfides (LiPSs), shuttle effect, redox kinetics, selenium vacancy, sulfur catalysis

1 Introduction

Advances in electronics and electric vehicles call for higher-energy-density energy storage and conversion devices [1–3]. Compared to the current commercial lithium-ion batteries, lithium-sulfur (Li-S) batteries are considered as a potential alternative to avoid the limitation of cathode capacity and anode mismatch in lithium-ion batteries due to the high theoretical capacity (1,675 mAh·g^{-1}) and energy density (2,600 Wh·kg^{-1}) [4, 5]. Moreover, the low cost and non-toxic nature of sulfur offer economic benefits and environmental friendliness. Unfortunately, several technical challenges still hamper the advancement of Li-S batteries, such as the inherent poor electronic conductivity of sulfur (5×10^{-30} S·cm^{-1} at room temperature), the undesirable large volume variation of the sulfur cathode (80%), as well as the dissolution of lithium polysulfides (LiPSs) with a notorious shuttle effect [6–8]. Together, these obstacles bring about fast capacity decay and poor rate performance of Li-S batteries.

In response to the aforementioned challenges, a typical strategy is encapsulating sulfur into porous carbonaceous materials for improving the cathode conductivity and relieving the LiPSs migration owing to the high conductivity and abundant pore structure [9, 10]. However, the intrinsically non-polar carbonaceous materials can only bind LiPSs within a few cycles through a weak van der Waals force, and then the battery capacity declines rapidly [11, 12]. Given this, polar transition metal oxides and sulfides have drawn increasing attention as potential sulfur hosts owing to the strong LiPSs anchoring ability [13, 14]. Unfortunately, most of these materials still do not meet the practical requirements of Li-S batteries, especially in high sulfur contents or poor electrolyte/sulfur (E/S) ratios due to the difficulty in anchoring excess LiPSs with oxides and sulfides [15]. Recently, introducing electrocatalysts to facilitate sulfur species conversion has been considered as a valid strategy to improve the rate and cycle performance of Li-S batteries given the multi-electron redox reactions that occur during the cycle [16–18].

Layered transition metal selenium compounds possess attractive physical/chemical properties such as high specific surface area, impressive catalytic effect for sulfur conversion, and good compatibility with sulfur and lithium sulfide, showing great potential as sulfur hosts [19, 20]. Recent studies found that selenium and sulfur can form selenium-sulfur solid solution (Se_xS_y) bathing suit, thus improving the electrical conductivity and reactivity of sulfur [21]. Bismuth selenide (Bi_2Se_3), with a desirable interfacial charge feature and narrow bandgap of 0.3 eV, has been widely studied in the field of thermoelectric and optoelectronic devices [22]. In particular, its two-dimensional layered structure and desirable interfacial charge feature make it widely studied in the electrode materials of both lithium-ion batteries and sodium-

Address correspondence to Gongming Wang, wanggm@ustc.edu.cn; Minghua Chen, mhchen@hrbust.edu.cn

ion batteries [23]. These advantages make Bi_2Se_3 promising in catalytic and stable sulfur electrochemistry. However, the catalytical active sites in two-dimensional materials are mainly concentrated at the edges, and the basal planes are almost inert to catalyze redox reactions [24–26]. In this regard, the strategy of anionic vacancy design has been proposed to further enhance the electrochemical performance of two-dimensional materials [23, 27, 28]. The rationally introduced anionic vacancies can optimize the band structure, charge distribution, and crystal structure of the target materials and thus improve their intrinsic properties such as electronic/ionic transportation properties, adsorption ability, catalytic activity, and structural durability. Therefore, introducing anionic vacancy may also be an effective way to enhance the electrochemical performance of Bi_2Se_3 as a sulfur host. Although the enhanced mechanism of anionic vacancies has been widely explored [17, 28], the influence of anionic vacancies on the sulfur redox reaction process in Li-S batteries has not been well understood, especially for Se vacancy.

Considering this, a series of heterogeneous composites (Bi_2Se_{3-x}/NC) with adjustable Se vacancy contents are developed by selenizing Bi-based metal-organic framework (Bi-MOFs) precursor and subsequent thermal shock, and employed as sulfur host. Bi_2Se_{3-x} with different numbers of selenium vacancies was also prepared quantitatively by controlling the annealing temperature and time. The MOFs-derived porous nitrogen-doped carbon can inhibit volume expansion of sulfur electrodes, localize sulfur species, and offer abundant active interfaces for electronic transmission. Meanwhile, defect engineering and structure features not only endow Bi_2Se_{3-x} with enhanced conductivity and sulfophilic property but also promote the conversion reaction of sulfur species, which allows for effective shuttle suppression and fast sulfur redox kinetics. In addition, Bi_2Se_{3-x} with the suitable amount of selenium vacancies achieves the best electrochemical performance due to the advantages of its structure and composition. These results confirm the intrinsic correlation between defects and catalysis, which are revealed by computational and experimental studies. As a result, Bi_2Se_{3-x} host exhibits admirable stability with a fairly lower capacity decay rate of approximately 0.0278% per cycle over 1,000 cycles at a 3 C rate, and still demonstrates a high discharge capacity of 455 $mAh \cdot g^{-1}$ at 1 C even at a high sulfur content of 6.2 $mg \cdot cm^{-2}$. This work uncovers the enhanced mechanism of Se vacancy and may enlighten the development of anionic vacancies toward high-performance Li-S batteries.

2 Results and discussion

Figure 1(a) illustrates the synthesis route of Bi_2Se_{3-x}/NC heterogeneous composites. In particular, Bi-MOFs precursor is synthesized by simple hydrothermal method, and then selenized and pyrolyzed to obtain two-dimensional Bi_2Se_3 nanosheets and nitrogen-doped composites. Finally, defect-rich Bi_2Se_{3-x}/NC is produced by the following thermal shock process. The field emission scanning electron microscopy (SEM) images display the uniform morphology and structure of Bi-MOFs (Fig. 1(b)), Bi_2Se_3/NC (Fig. 1(c)), and Bi_2Se_{3-x}/NC (Fig. 1(d)), respectively.

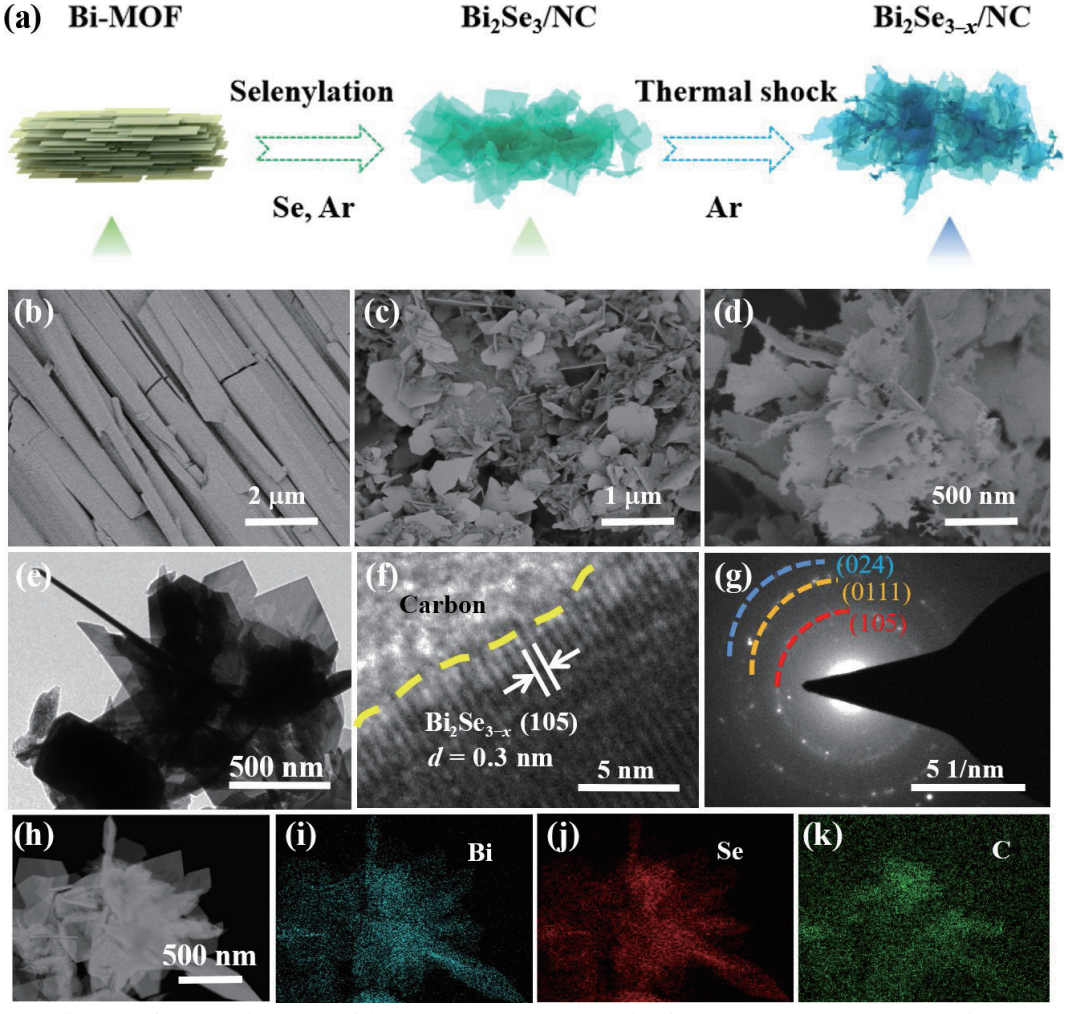

Figure 1 (a) Scheme illustration for the synthetic route of the Bi_2Se_{3-x}/NC. SEM micrographs of (b) Bi-MOFs, (c) Bi_2Se_3/NC, and (d) Bi_2Se_{3-x}/NC. (e) TEM, (f) HRTEM, and (g) SAED images of Bi_2Se_{3-x}/NC. (h)–(k) EDS elemental mapping of Bi_2Se_{3-x}/NC.

Indeed, the nanosheet structure of Bi_2Se_3 appears after selenizing Bi-MOFs. Interestingly, the edge of Bi_2Se_{3-x} nanosheets is more exposed than Bi_2Se_3 nanosheets via further thermal shock to introduce selenium vacancies, which is more favorable for anchoring and catalyzing sulfur species for suppressing the shuttle effect toward high-performance Li-S batteries. The Bi_2Se_{3-x}/NC/sulfur (Bi_2Se_{3-x}/NC/S) composite is prepared by the melt-impregnation method. SEM images show that the edge-rich morphology of Bi_2Se_{3-x}/NC is well maintained after infiltration of sulfur (Fig. S1(a) in the Electronic Supplementary Material (ESM)). The two-dimensional Bi_2Se_{3-x} can still be observed through transmission electron microscopy (TEM) (Fig. 1(e)). Moreover, the high-resolution TEM (HRTEM) image displays the Bi_2Se_{3-x}/NC composites consisting of Bi_2Se_{3-x} nanosheets with the clear lattice fringes (a *d*-spacing of 0.304 nm allocated to the (105) plane of Bi_2Se_3 crystal) and nitrogen-doped carbon derived from the ligands in Bi-MOFs (Fig. 1(f)). Similarly, Bi_2Se_{3-x} can be calibrated by observing the lattice constants in the corresponding selected area electron diffraction (SAED) diagram as shown in Fig. 1(g). Additionally, the homogeneous distribution of Bi, Se, and C in the Bi_2Se_{3-x}/NC composites is characterized by the energy dispersive X-ray spectrometer (EDS) elemental mapping in Figs. 1(h)–1(k).

To reveal the inherent physical and chemical advantages of the defect-rich Bi_2Se_{3-x}/NC, a series of characterization methods are used to study and compare the related properties of the two samples. X-ray diffraction (XRD) is employed to study the effect of defect engineering on the crystallization and composition properties of the samples. As shown in Fig. 2(a), both Bi_2Se_3/NC and Bi_2Se_{3-x}/NC demonstrate a series of sharp diffraction peaks matching the Bi_2Se_3 phase (PDF#89-2008) in good condition, suggesting their crystal structures are consistent with the HRTEM results. Remarkably, magnified XRD patterns of Bi_2Se_3/NC and Bi_2Se_{3-x}/NC also display the left-shifted peak and increased peak value of Bi_2Se_{3-x}/NC compared with Bi_2Se_3/NC (Fig. 2(b)), especially in the small-angle range, which is explained as the influence of selenium vacancies. The chemical states of Bi_2Se_3/NC and Bi_2Se_{3-x}/NC are ascertained by X-ray photoelectron spectroscopy (XPS). Bi, Se, C, N, and O five elements are present in Bi_2Se_{3-x}/NC composites revealed by the XPS survey spectrum in Fig. S2(a) in the ESM. As shown in Fig. 2(d), two typical peaks can be observed in the high-resolution Bi 4f XPS spectra of Bi_2Se_3/NC at 158 and 163.3 eV, corresponding to Bi $4f_{7/2}$ and $4f_{5/2}$, respectively. In comparison, Bi_2Se_{3-x}/NC shows a pair of peaks at 157.7 and 163 eV, displaying the slightly negative shift of 0.3 eV, which is attributed to the increased electron cloud density of the Bi atom due to the reduced Se coordination [29]. Moreover, the Se 3d high-resolution spectra for Bi_2Se_3/NC and Bi_2Se_{3-x}/NC are demonstrated in Fig. 2(e). The two typical peaks at 54.3 and 53.4 eV are assigned to the $3d_{3/2}$ and $3d_{5/2}$ levels of Se^{2-}, respectively. Meanwhile, the typical peak at 55.9 eV is thought to form the Bi–Se bond. In contrast, a new Se^0 peak at 56.8 eV for Bi_2Se_{3-x}/NC confirms the introduction and increase of selenium vacancies with the thermal shock process [30]. Additionally, N 1s

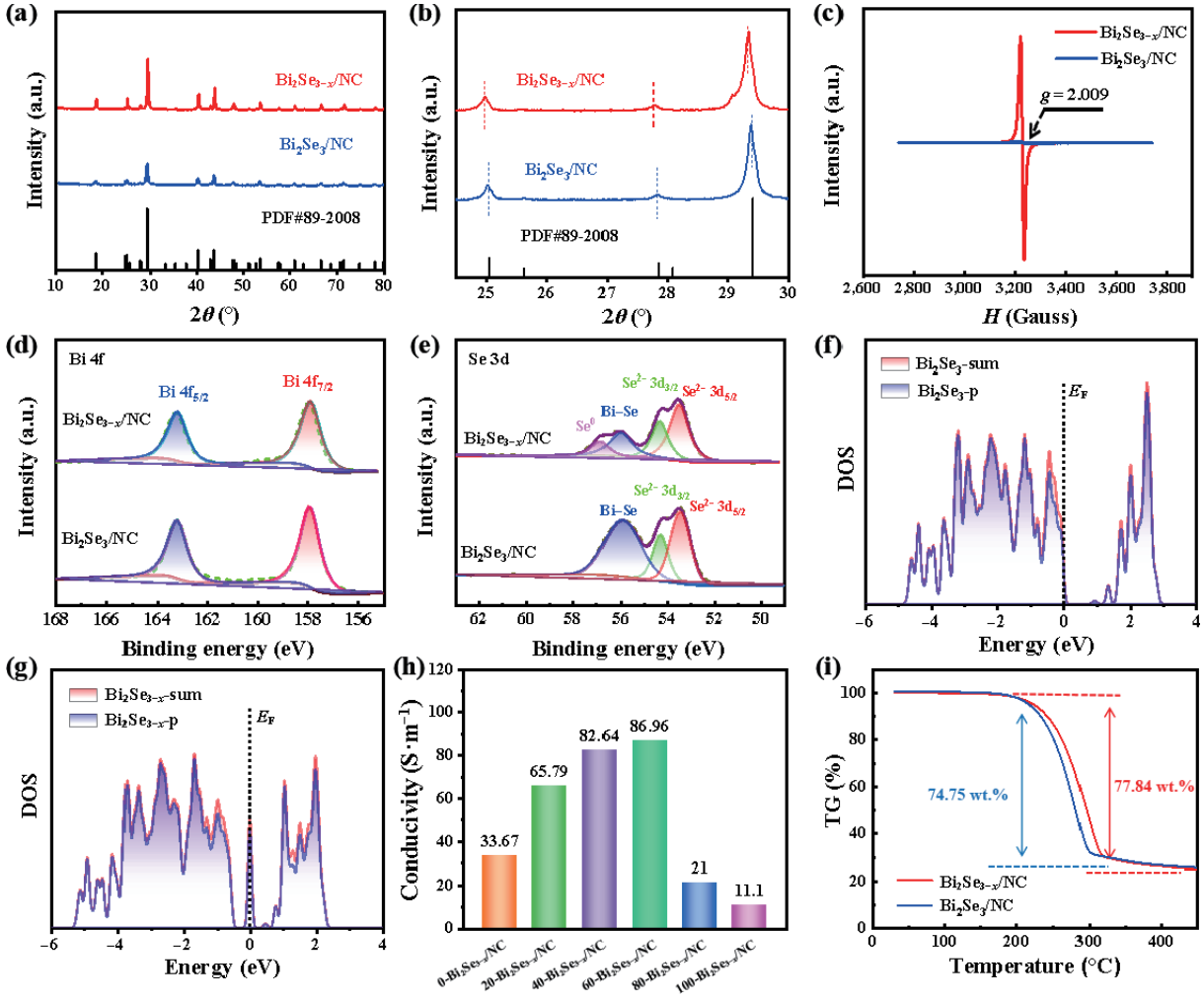

Figure 2 (a) XRD patterns; (b) Magnified XRD patterns. (c) EPR spectra. (d) Bi 4f and (e) Se 3d high-resolution XPS spectra of Bi_2Se_3/NC and Bi_2Se_{3-x}/NC; DOS plots of surface p-band and sum for (f) Bi_2Se_3/NC and (g) Bi_2Se_{3-x}/NC. (h) Conductivities of different *a*-Bi_2Se_{3-x}/NC samples. (i) TGA curves of Bi_2Se_{3-x}/NC/S and Bi_2Se_3/NC/S composites.

spectrum attested to the existence of pyridinic-N at 398.5 eV, nitrile-N at 400 eV, pyrrolic-N at 401.2 eV, graphitic-N at 402.9 eV, and oxidized-N at 404.2 eV (Fig. S2(b) in the ESM). Besides, C 1s spectra are divided into three peaks, namely, C–C (284.8 eV), C–N (287 eV), and O=C–N (288.5 eV) (Fig. S2(c) in the ESM). These results further confirm that Bi_2Se_{3-x}/NC is successfully synthesized. The electron paramagnetic resonance (EPR) test is employed to further confirm the defect characteristic of Bi_2Se_{3-x}/NC composites. The EPR spectrum displays a sharp EPR signal at g value 2.009 for Bi_2Se_{3-x}/NC compared with the flat spectrum of Bi_2Se_3/NC in response to the presence of abundant selenium vacancies generated during the preparation process, which is shown in Fig. 2(c). Moreover, Figs. 2(f) and 2(g) depict the density of state (DOS) mode of Bi_2Se_3 and Bi_2Se_{3-x} simulated by first-principles calculations according to the electron distributions of Bi_2Se_{3-x} and Bi_2Se_3. The bandgap of Bi_2Se_{3-x} is significantly narrowed after the introduction of selenium vacancies. Distinctly, there exist prominent impurity states at the Fermi level of Bi_2Se_{3-x}, indicating that electrons might cross the Fermi level and the electronic conductivity is improved accordingly. All the above results determine that the electronic structure of Bi_2Se_3 changes significantly after the successful elimination of partial Se, and the electron distribution around the Bi atom is optimized, thus enhancing the adsorption and catalytic effect for the promoted performance of Li-S batteries.

Given the above results, the a-Bi_2Se_{3-x}/NC (a = 0, 20, 40, 60, 80, and 100) with different selenium vacancies levels are prepared by changing the thermal shock time to study the effect of selenium vacancies on the crystallization and composition of the product. Table S1 in the ESM summarizes the ratio of Se atoms to Bi atoms in samples with different defect levels. The atomic ratio continues to decrease from Bi_2Se_3/NC to 100-Bi_2Se_{3-x}/NC, which confirms the increase of selenium vacancies upon defect introduction. As depicted in Fig. S3 in the ESM, the XRD results show that the XRD peak of 0-Bi_2Se_3/NC matches the Bi_2Se_3 phase (PDF#89-2008) completely. When the thermal shock time increases to 60 min, the corresponding peaks are shifted to the left in turn, indicating the presence of selenium vacancies and its increased content in Bi_2Se_{3-x}/NC. As the thermal shock continues to increase, the crystal integrity of Bi_2Se_3 is constantly damaged, while new phase Bi metal appears until the thermal shock time of 100 min, indicating that excessive thermal shock resulted in the reduction of a large amount of Bi_2Se_3. In addition, the conductivities of a-Bi_2Se_{3-x}/NC with different selenium vacancies levels are tested, showing that the conductivity of 60-Bi_2Se_{3-x}/NC is the highest in a series of samples, which is more favorable for electrons/ions transport and sulfur species redox reactions (Fig. 2(h)). Therefore, 60-Bi_2Se_{3-x}/NC is employed as the best defect product for further study, labeled as Bi_2Se_{3-x}/NC.

To investigate the practical effect of Bi_2Se_{3-x}/NC as a sulfur host, the composite cathode electrodes (Bi_2Se_3/NC/S and Bi_2Se_{3-x}/NC/S) were prepared by melt impregnation process. As shown in Fig. 2(i), the thermal gravimetric analysis (TGA) test reveals the elemental sulfur loading in contrast sample and Bi_2Se_{3-x}/NC/S is 74.75 and 77.84 wt.%, respectively. The high sulfur loading results from the porous structure of Bi_2Se_{3-x}/NC that provides more sufficient space for sulfur. Moreover, Bi_2Se_{3-x}/NC has a higher sulfur release temperature, indicating that selenium vacancies enhance the adsorption of sulfur [31]. In addition, energy dispersive X-ray (EDX) elemental mapping of Bi_2Se_{3-x}/NC/S composite manifests that the element sulfur is evenly distributed in Bi_2Se_{3-x}/NC, which further indicates that Bi_2Se_{3-x}/NC/S was synthesized by the melt impregnation process (Fig. S4 in the ESM).

Button batteries (CR2032) with different hosts were assembled in an argon glove box and evaluated for performance. Figure 3(a) displays typical cyclic voltammetry (CV) curves for the Bi_2Se_{3-x}/NC/S electrode at 0.1 mV·s^{-1} rate with two clear oxidation peaks interpreted as the conversion of short-chain sulfur species to long-chain sulfur species, and the two reduction peaks represented the conversion of long-chain sulfur species to short-chain sulfur species. Apparently, the CV curves of the first three cycles of Bi_2Se_{3-x}/NC/S almost coincide, which implies the stable and reversible operation of the sulfur cathode. As shown in Fig. S5 in the ESM, compared with the CV curves of Bi_2Se_3/NC/S, the two reduction peaks move positively coupled with the two oxidation peaks moving negatively, indicating that Bi_2Se_{3-x}/NC offers less overpotential for sulfur species transformation. Figure 3(b) demonstrates the charge–discharge curves of the typical number of cycles of Bi_2Se_{3-x}/NC/S at 0.1 C. The two discharge voltage platforms correspond to the conversion of sulfur to LiPSs, and then to Li_2S, while the charge voltage platform corresponds to the reverse process. The reaction platforms remain in good condition after 100 cycles, indicating favorable stability. The galvanostatic cycling curves at 0.1 C are presented in Fig. 3(c). By comparison, the maintained capacity of the Bi_2Se_{3-x}/NC/S electrode is 205 mAh·g^{-1} higher than that of Bi_2Se_3/NC/S after 100 cycles, which demonstrates the satisfactory sulfur-fixation capacity and easy redox kinetics brought about by defect engineering. Furthermore, the two electrodes are subjected to a long-term cycle performance test at 3 C for 1,100 cycles to further demonstrate the effect of defect engineering on cycle stability. As displayed in Fig. 3(e), the Bi_2Se_{3-x}/NC/S electrode exhibits more admirable stability and a fairly lower capacity decay rate of approximately 0.0278% per cycle than 0.06% of Bi_2Se_3/NC/S. In addition, Fig. 3(d) demonstrates the superior rate performance of the Bi_2Se_{3-x}/NC/S electrode which exhibits 435 mAh·g^{-1} at 5 C and remains at 847 mAh·g^{-1} when return to 0.2 C, further manifesting the remarkable stability and highly reversibility of Bi_2Se_{3-x}/NC/S. In addition, the cycling performance based on a-Bi_2Se_{3-x}/NC/S at different defect levels is compared (Fig. S6 in the ESM), among which 60-Bi_2Se_{3-x}/NC/S achieves the highest capacity and optimal cycling performance caused by its modest selenium vacancies level, outstanding electrical conductivity, and complete internal structure.

The realization of high energy density Li-S batteries calls for increasing cathode sulfur loading and decreasing electrolyte consumption. Given this, the cyclic performance of Bi_2Se_{3-x}/NC/S with increasing sulfur loadings of 1.3, 2.9, and 6.2 mg·cm^{-2} is tested over 100 cycles at 0.2 C. Thanks to the strong adsorption and superior charge transfer properties of Bi_2Se_{3-x}/NC, their initial discharge capacity, retentive capacity, and capacity decay rate after 100 cycles of Bi_2Se_{3-x}/NC/S with a 1.3 mg·cm^{-2} sulfur content are 1,065.86 mAh·g^{-1}, 505.85 mAh·g^{-1}, and 0.5%; 2.9 mg·cm^{-2} were 1,118.52 mAh·g^{-1}, 644.18 mAh·g^{-1}, and 0.4%; 6.2 mg·cm^{-2} were 1,169.12 mAh·g^{-1}, 808.35 mAh·g^{-1}, and 0.3% (Fig. S7 in the ESM). The rate performance of Bi_2Se_{3-x}/NC/S is also examined with a 6.2 mg·cm^{-2} sulfur content (Fig. 3(f)). The Bi_2Se_{3-x}/NC/S still demonstrates a discharge capacity of 455 mAh·g^{-1} at a 1 C rate coupled with a little change of discharge capacity when the rate returns to 0.2 C compared with the initial 0.2 C, suggesting that the electrode still offers excellent stability and reversibility even under high sulfur loading. Moreover, as shown in Fig. 3(g), the typical two platforms are still visible in the galvanostatic discharge–charge curves of the Bi_2Se_{3-x}/NC/S with a 6.2 mg·cm^{-2} sulfur content benefiting from the unique selenium vacancies design in Bi_2Se_{3-x}/NC. These results further confirm the significant advantages of the Bi_2Se_{3-x}/NC design in the pursuit of high-performance Li-S batteries. As a demonstration of practical application, the battery with Bi_2Se_{3-x}/NC is capable of powering

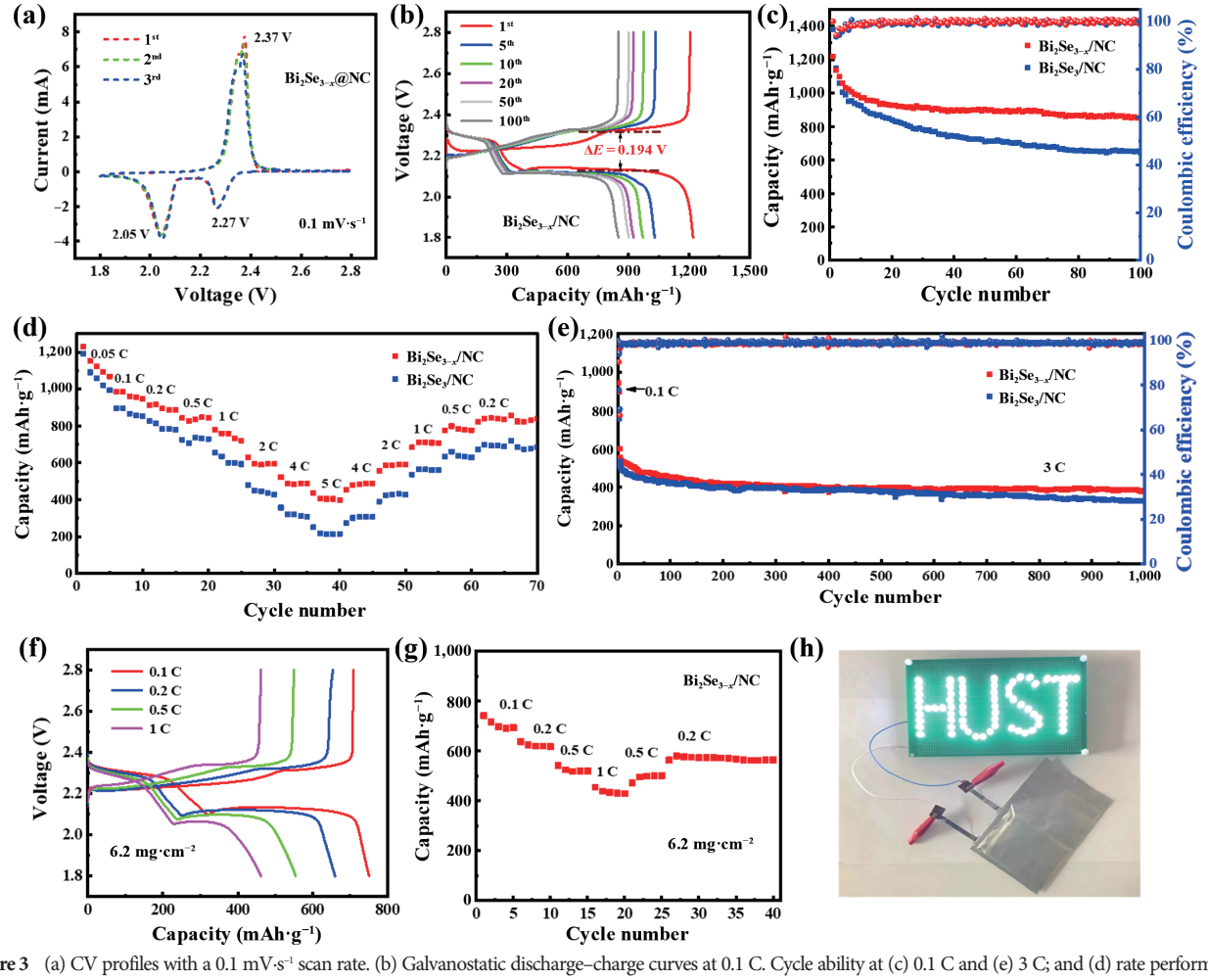

Figure 3 (a) CV profiles with a 0.1 mV·s^{-1} scan rate. (b) Galvanostatic discharge–charge curves at 0.1 C. Cycle ability at (c) 0.1 C and (e) 3 C; and (d) rate performance of the cell with the Bi_2Se_{3-x}/NC and Bi_2Se_3/NC. (f) Galvanostatic discharge–charge profiles and (g) rate performance of cells with Bi_2Se_{3-x}/NC under 6.2 mg·cm^{-2} sulfur content. (h) Photograph of light emitting diodes powered by soft package battery with Bi_2Se_{3-x}/NC.

light-emitting diodes (Fig. 3(h)), indicating good energy storage capability and bright application prospects.

To understand the potential mechanism of electrode electrochemical improvement of Bi_2Se_{3-x}/NC, we employ density functional theory (DFT) to clarify its optimized electron states and excellent charge transport properties. The top-view and side-view structures of Bi_2Se_3 and Bi_2Se_{3-x} are shown in Fig. S9 in the ESM. Figure S10 in the ESM depicts the computational simulations of the interactions between Bi_2Se_{3-x} (or Bi_2Se_3) and sulfur species regarding the full sulfurization state during battery charging and discharging. The adsorption energies of each sulfur species on the (101) lattice plane of Bi_2Se_{3-x} and Bi_2Se_3 are calculated as shown in Fig. 4(a). Specifically, the adsorption energies of S_8, Li_2S_8, Li_2S_6, Li_2S_4, Li_2S_2, and Li_2S on Bi_2Se_{3-x} surface are +0.18, −0.16, −0.60, −1.70, −1.73, and −2.73 eV, respectively, which all higher than those on Bi_2Se_3 surface are +0.57, −0.12, −0.11, −0.23, −0.83, and −1.53 eV, respectively. This result confirms the tremendous ability of defect engineering to enhance LiPSs adsorption for sulfur electrochemistry. The transformation of soluble Li_2S_4 to insoluble Li_2S_2/Li_2S is a key step, thereby Li_2S_4 is a significant intermediate to illuminate the electrochemical interaction of Bi_2Se_3/NC or Bi_2Se_{3-x}/NC on LiPSs [32]. As shown in Fig. 4(b), according to the differences of electron density between the two samples for the adsorption structure of Li_2S_4, the surface electrostatic potential plots were employed to reveal the surface chemical interaction. Based on the calculation results, the interaction between the S atom and Bi atom dominated the main adsorption behavior of Li_2S_4, and a powerful Bi–S bond is formed due to the electrons of the S atoms prefer to flow toward the Bi atoms. In fact, the charge transfer amount between Bi and S on the Bi_2Se_{3-x} surface is more than that on Bi_2Se_3. The surface charge density and surface differential charge density are calculated to indicate more electrons flowed in/out of Bi_2Se_{3-x} surface and charge accumulation around selenium vacancies, which indicates that selenium vacancies promote the electron contacts between Bi_2Se_{3-x} and sulfur species, thus enhancing the polar adsorption of Bi_2Se_{3-x}/NC (Fig. 4(c)). In addition, the kinetic process of Li_2S decomposition has been studied based on the climbing image nudged elastic band (CI-NEB) method, which is given in Fig. 4(d). The Li_2S decomposition has a much lower energy barrier of 0.02 eV on the selenium vacancies-rich Bi_2Se_{3-x} surface than that on pristine Bi_2Se_3 (0.54 eV), indicating the facilitated Li_2S transformation kinetics thanks to the superiority of selenium vacancies. Together, the DFT results show that the defective Bi_2Se_{3-x} holds a broad prospect as an efficient sulfur electrocatalyst.

Selenium defect and optimized electronic structure enable the as-designed Bi_2Se_{3-x}/NC to exhibit strong sulfur constraints and fast redox kinetics (Fig. 5(a)). The superior LiPSs adsorption of the Bi_2Se_{3-x}/NC can be further visualized by immersing the same amount of Bi_2Se_{3-x}/NC and Bi_2Se_3/NC in the 1,2-dimethoxyethane:1,3-dioxolane (DME:DOL, 1:1) solution of 0.05 M Li_2S_6 and standing for 2 h to observe the superior LiPSs adsorption performance of Bi_2Se_{3-x}/NC (Fig. S8 in the ESM). Apparently, the color of the Bi_2Se_{3-x}/NC-Li_2S_6 solution gradually changed from brown to nearly transparent after 2 h, while the color of Bi_2Se_3/NC-Li_2S_6 solution still remained distinctly brown, exhibiting a strong visual absorption effect realized by Bi_2Se_{3-x}/NC (Fig. 5(b)). In addition, symmetrical cells based on Bi_2Se_3/NC and

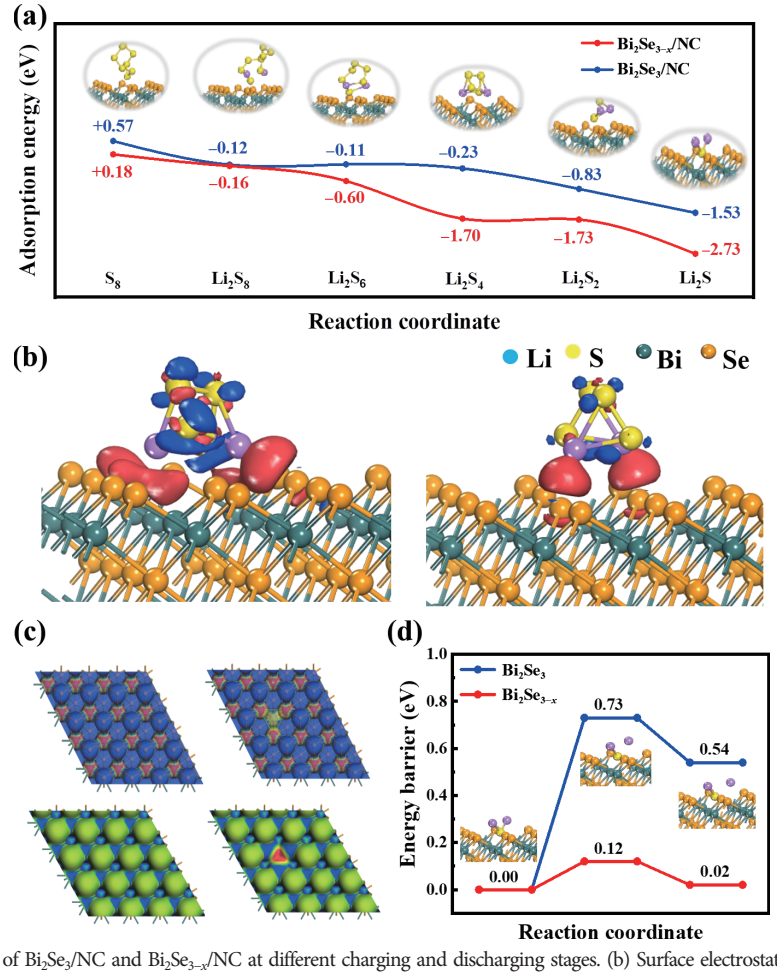

Figure 4 (a) Adsorption energy of Bi_2Se_3/NC and Bi_2Se_{3-x}/NC at different charging and discharging stages. (b) Surface electrostatic potential diagram based on the electron density difference of Li_2S_4 on Bi_2Se_{3-x} (left) and Bi_2Se_3 (right). (c) Surface charge density distribution (up) and surface differential charge density distribution (down) of Bi_2Se_3 (left) and Bi_2Se_{3-x} (right). (d) Decomposition energy distribution of Li_2S clusters on Bi_2Se_3 and Bi_2Se_{3-x}.

Bi_2Se_{3-x}/NC serve as a proof-of-concept to compare and evaluate the catalytic ability of the as-designed Bi_2Se_{3-x}/NC [33]. Based on the multi-step conversion reaction mechanism of sulfur electrochemistry, CV curves of symmetric batteries at different scanning rates of 0.1–0.5 mV·S^{-1} were studied, which are exhibited in Figs. 5(c) and 5(d). With the increase of scanning rate, the anodic peaks in the cathode had a significant positive move, while the cathodic peaks had an opposite move, resulting in an increasing polarization voltage at higher scanning rates. By contrast, the two redox peaks of Bi_2Se_{3-x}/NC/S moved slightly with the increasing scanning rates, indicating the fast and facilitated sulfur redox reaction. To further investigate the superiority of Bi_2Se_{3-x}/NC to sulfur species conversion kinetics, we investigated the corresponding lithium-ion diffusion properties. The Li-ion diffusion coefficient can be estimated from the classical Randles–Sevcik equation

$$I_p = (2.69 \times 10^5) n^{0.5} A D^{0.5} C v^{0.5} \quad (1)$$

where I_p is the peak current, n is the number of reacting electrons, A is the electrode area, D is the diffusion coefficient of lithium ions, C is the concentration of lithium ions in the electrolyte, and v is the scanning rate. Given this, all reduction and oxidation peaks are linear with the square root of the scanning rate [34–36]. The slope of the Bi_2Se_{3-x}/NC/S electrode is higher than that of the Bi_2Se_3/NC/S electrode in each sulfur redox reaction, indicating faster Li-ion diffusion rate and improved sulfur redox kinetics during cycling (Figs. 5(e) and 5(f)). Electrochemical impedance spectroscopy (EIS) spectra revealed that the Bi_2Se_{3-x}/NC symmetric cell has a smaller electrochemical resistance, which is consistent with the density of states calculated above (Fig. 5(g)). This is prone to sulfur redox reactions. 75% of the discharge capacity of Li-S batteries is determined by the solid–liquid conversion from Li_2S_4 to Li_2S. Therefore, the nucleation-deposition of Li_2S on the electrode plays an important role in the overall sulfur reaction. To further investigate the outstanding catalytic effect of Bi_2Se_{3-x}/NC, the so-called nucleation-deposition experiment was carried out based on Bi_2Se_{3-x}/NC electrodes and Li_2S_8/tetraglyme electrolyte, and the potentiostatic discharge profiles of different cells are shown in the Fig. 5(h) [13, 37, 38]. The value of the line integral of current indicates the ability of nucleation deposition of Li_2S. Thereby, the capacity of Li_2S deposition on Bi_2Se_{3-x}/NC surface is distinctly higher than that of Bi_2Se_{3-x}/NC, which further proves that Bi_2Se_{3-x}/NC has a distinctly catalytic effect on the sulfur reaction. Altogether, the above results demonstrate the excellent anchoring ability and catalytic activity of Bi_2Se_{3-x}/NC owing to the structure construction and defect engineering toward expedited and stable Li-S electrochemistry.

3 Conclusions

In conclusion, the narrow-bandgap Bi_2Se_{3-x}/NC with different selenium vacancies amounts was developed via a selenization pyrolysis followed by a thermal shock process. The experimental results and DFT investigation infer that selenium deficiencies give Bi_2Se_{3-x}/NC improved electronic conductivity, enhanced sulfur affinity, and optimized catalytic activity, which not only inhibits shuttle behavior of LiPSs, but also promotes sulfur redox kinetics. Combined with the highly-conductive porous N doped carbon derived from the pyrolysis of Bi-MOF precursor, Bi_2Se_{3-x}/NC/S

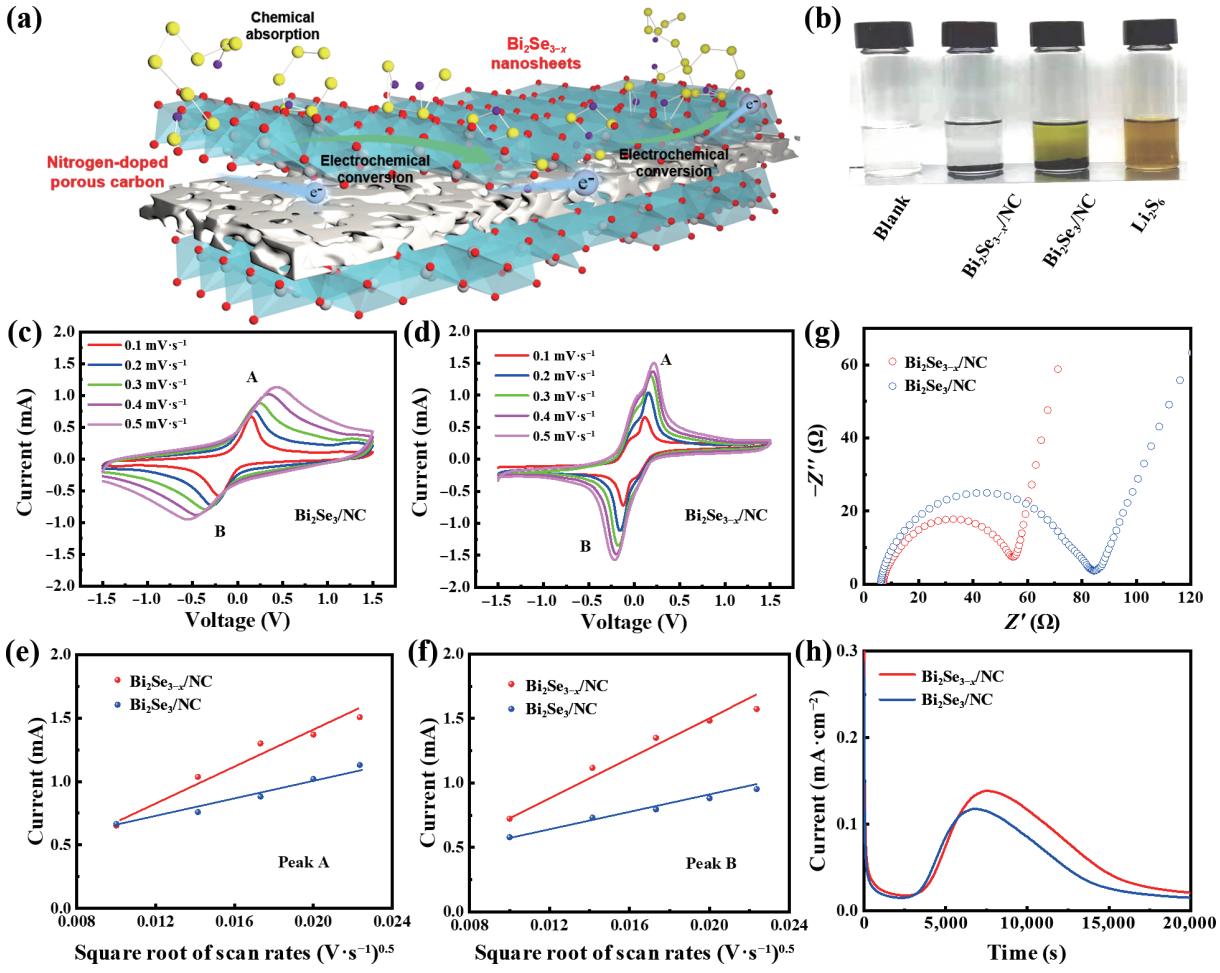

Figure 5 (a) Scheme illustration of sulfur species chemical adsorption and catalytic conversion of Bi_2Se_{3-x}/NC. (b) Optical images of Li_2S_6 adsorption test. (c) and (d) CV curves of symmetric cells with Bi_2Se_3/NC/S and Bi_2Se_{3-x}/NC/S electrode. (e) and (f) CV peak current values of peaks A and B for Bi_2Se_3/NC/S and Bi_2Se_{3-x}/NC/S electrode versus the square root of scan rates. (g) EIS spectra of symmetric cells with Bi_2Se_3/NC and Bi_2Se_{3-x}/NC electrodes. (h) Potentiostatic Li_2S deposition curves of Bi_2Se_3/NC and Bi_2Se_{3-x}/NC electrode.

cathode contributes to a fairly lower capacity decay rate of approximately 0.0278% per cycle over 1,000 cycles at 3 C. Even at the high sulfur loading of 6.2 mg·cm^{-2}, the cathode still demonstrates a discharge capacity of 455 mAh·g^{-1} at 1 C. Our work completes the enhanced mechanism of Se vacancy and may facilitate the development of anionic vacancy as well as high-performance Li-S batteries.

Acknowledgements

This work was supported by the National Natural Science Foundation of China (No. 52122702), the Natural Science Foundation of Heilongjiang Province of China (No. JQ2021E005), and the Fundamental Research Foundation for Universities of Heilongjiang Province (No. LGYC2018JQ006).

Electronic Supplementary Material: Supplementary material (experimental section, supplementary characterization and electrochemical performances) is available in the online version of this article at https://doi.org/10.1007/s12274-022-4453-9.

References

[1] Sun, F.; Osenberg, M.; Dong, K.; Zhou, D.; Hilger, A.; Jafta, C. J.; Risse, S.; Lu, Y.; Markötter, H.; Manke, I. Correlating morphological evolution of Li electrodes with degrading electrochemical performance of Li/$LiCoO_2$ and Li/S battery systems: Investigated by synchrotron X-ray phase contrast tomography. *ACS Energy Lett.* **2018**, *3*, 356–365.

[2] Chen, M. H.; Fan, H.; Zhang, Y.; Liang, X. Q.; Chen, Q. G.; Xia, X. H. Coupling PEDOT on mesoporous vanadium nitride arrays for advanced flexible all-solid-state supercapacitors. *Small* **2020**, *16*, 2003434.

[3] Liang, X. Q.; Chen, M. H.; Zhu, H. K.; Zhu, H.; Cui, X. H.; Yan, J. X.; Chen, Q. G.; Xia, X. H.; Liu, Q. Unveiling the solid-solution charge storage mechanism in 1T vanadium disulfide nanoarray cathodes. *J. Mater. Chem. A* **2020**, *8*, 9068–9076.

[4] Ji, X. L.; Lee, K. T.; Nazar, L. F. A highly ordered nanostructured carbon-sulphur cathode for lithium-sulphur batteries. *Nat. Mater.* **2009**, *8*, 500–506.

[5] Bruce, P. G.; Freunberger, S. A.; Hardwick, L. J.; Tarascon, J. M. Li-O_2 and Li-S batteries with high energy storage. *Nat Mater.* **2011**, *11*, 19–29.

[6] Hwang, J. Y.; Shin, S.; Yoon, C. S.; Sun, Y. K. Nano-compacted Li_2S/graphene composite cathode for high-energy lithium-sulfur batteries. *ACS Energy Lett.* **2019**, *4*, 2787–2795.

[7] He, J. R.; Manthiram, A. A review on the status and challenges of electrocatalysts in lithium-sulfur batteries. *Energy Stor. Mater.* **2019**, *20*, 55–70.

[8] Lim, W. G.; Kim, S.; Jo, C.; Lee, J. A comprehensive review of materials with catalytic effects in Li-S batteries: Enhanced redox kinetics. *Angew. Chem., Int. Ed.* **2019**, *58*, 18746–18757.

[9] Kang, H. S.; Park, E.; Hwang, J. Y.; Kim, H.; Aurbach, D.; Rosenman, A.; Sun, Y. K. Li-S batteries: A scaled-up lithium (ion)-sulfur battery: Newly faced problems and solutions. *Adv. Mater. Technol.* **2016**, *1*, 1600052.

[10] Jiang, Y.; Liu, H. Q.; Tan, X. H.; Guo, L. M.; Zhang, J. T.; Liu, S. N.; Guo, Y. J.; Zhang, J.; Wang, H. F.; Chu, W. G. Monoclinic ZIF-8 nanosheet-derived 2D carbon nanosheets as sulfur immobilizer for

high-performance lithium sulfur batteries. *ACS Appl. Mater. Interfaces* **2017**, *9*, 25239–25249.

[11] Salhabi, E. H. M.; Zhao, J. L.; Wang, J. Y.; Yang, M.; Wang, B.; Wang, D. Hollow multi-shelled structural TiO_{2-x} with multiple spatial confinement for long-life lithium-sulfur batteries. *Angew. Chem. , Int. Ed.* **2019**, *58*, 9078–9082.

[12] Li, Z. Q.; Yin, L. W. Nitrogen-doped MOF-derived micropores carbon as immobilizer for small sulfur molecules as a cathode for lithium sulfur batteries with excellent electrochemical performance. *ACS Appl. Mater. Interfaces* **2015**, *7*, 4029–4038.

[13] Jin, Z. S.; Zhao, M.; Lin, T. N.; Liu, B. Q.; Zhang, Q.; Zhang, L. Y.; Chen, L. H.; Li, L.; Su, Z. M.; Wang, C. G. Rational design of well-dispersed ultrafine CoS_2 nanocrystals in micro-mesoporous carbon spheres with a synergistic effect for high-performance lithium-sulfur batteries. *J. Mater. Chem. A* **2020**, *8*, 10885–10890.

[14] Chen, M. H.; Li, T. Y.; Li, Y.; Liang, X. Q.; Sun, W. F.; Chen, Q. G. Rational design of a MnO nanoparticle-embedded carbon nanofiber interlayer for advanced lithium-sulfur batteries. *ACS Appl. Energy Mater.* **2020**, *3*, 10793–10801.

[15] Lei, T. Y.; Chen, W.; Huang, J. W.; Yan, C. Y.; Sun, H. X.; Wang, C.; Zhang, W. L.; Li, Y. R.; Xiong, J. Multi-functional layered WS_2 nanosheets for enhancing the performance of lithium-sulfur batteries. *Adv. Energy Mater.* **2017**, *7*, 1601843.

[16] Qiu, S. S.; Liang, X. Q.; Li, Y.; Xia, X. H.; Chen, M. H. Recent advance on Co-based materials for polysulfide catalysis toward promoted lithium-sulfur batteries. *Nano Select* **2022**, *3*, 298–319.

[17] Li, X. X.; Gao, B.; Huang, X.; Guo, Z. J.; Li, Q. W.; Zhang, X. M.; Chu, P. K.; Huo, K. F. Conductive mesoporous niobium nitride microspheres/nitrogen-doped graphene hybrid with efficient polysulfide anchoring and catalytic conversion for high-performance lithium-sulfur batteries. *ACS Appl. Mater. Interfaces* **2019**, *11*, 2961–2969.

[18] Zhou, G. M.; Zhao, S. Y.; Wang, T. S.; Yang, S. Z.; Johannessen, B.; Chen, H.; Liu, C. W.; Ye, Y. S.; Wu, Y. C.; Peng, Y. C.; et al. Theoretical calculation guided design of single-atom catalysts toward fast kinetic and long-life Li-S batteries. *Nano Lett.* **2020**, *20*, 1252–1261.

[19] Wang, M. X.; Fan, L. S.; Sun, X.; Guan, B.; Jiang, B.; Wu, X.; Tian, D.; Sun, K. N.; Qiu, Y.; Yin, X. J.; et al. Nitrogen-doped $CoSe_2$ as a bifunctional catalyst for high areal capacity and lean electrolyte of Li-S battery. *ACS Energy Lett.* **2020**, *5*, 3041–3050.

[20] Li, Y.; Chen, M. H.; Liu, B.; Zhang, Y.; Liang, X. Q.; Xia, X. H. Heteroatom doping: An effective way to boost sodium ion storage. *Adv. Energy Mater.* **2020**, *10*, 2000927.

[21] Yuan, H.; Peng, H. J.; Li, B. Q.; Xie, J.; Kong, L.; Zhao, M.; Chen, X.; Huang, J. Q.; Zhang, Q. Conductive and catalytic triple-phase interfaces enabling uniform nucleation in high-rate lithium-sulfur batteries. *Adv. Energy Mater.* **2019**, *9*, 1802768.

[22] Fang, R. P.; Zhao, S. Y.; Sun, Z. H.; Wang, D. W.; Cheng, H. M.; Li, F. More reliable lithium-sulfur batteries: Status, solutions and prospects. *Adv. Mater.* **2017**, *29*, 1606823.

[23] Shi, H. F.; Lv, W.; Zhang, C.; Wang, D. W.; Ling, G. W.; He, Y. B.; Kang, F. Y.; Yang, Q. H. Functional carbons remedy the shuttling of polysulfides in lithium-sulfur batteries: Confining, trapping, blocking, and breaking up. *Adv. Funct. Mater.* **2018**, *28*, 1800508.

[24] Zhang, Z. W.; Peng, H. J.; Zhao, M.; Huang, J. Q. Heterogeneous/homogeneous mediators for high-energy-density lithium-sulfur batteries: Progress and prospects. *Adv. Funct. Mater.* **2018**, *28*, 1707536.

[25] Li, Z. C.; Pan, H. L.; Wei, W. X.; Dong, A. L.; Zhang, K. L.; Lv, H. Y.; He, X. H. Bismuth metal-organic frameworks derived bismuth selenide nanosheets/nitrogen-doped carbon hybrids as anodes for Li-ion batteries with improved cyclic performance. *Ceram. Int.* **2019**, *45*, 11861–11867.

[26] Zheng, H. B.; Zeng, Y. X.; Zhang, H. Z.; Zhao, X. Y.; Chen, M. H.; Liu, J.; Lu, X. H. Oxygen vacancy activated Bi_2O_3 nanoflowers as a high-performance anode for rechargeable alkaline battery. *J. Power Sources* **2019**, *433*, 126684.

[27] Liu, Y. W.; Xiao, C.; Li, Z.; Xie, Y. Vacancy engineering for tuning electron and phonon structures of two-dimensional materials. *Adv. Energy Mater.* **2016**, *6*, 1600436.

[28] Zhang, Y. G.; Li, G. R.; Wang, J. Y.; Cui, G. L.; Wei, X. L.; Shui, L. L.; Kempa, K.; Zhou, G. F.; Wang, X.; Chen, Z. W. Hierarchical defective $Fe_{3-x}C$@C hollow microsphere enables fast and long-lasting lithium-sulfur batteries. *Adv. Funct. Mater.* **2020**, *30*, 2001165.

[29] Wang, J. Y.; Zhao, Y.; Li, G. R.; Luo, D.; Liu, J. B.; Zhang, Y. G.; Wang, X.; Shui, L. L.; Chen, Z. W. Aligned sulfur-deficient ZnS_{1-x} nanotube arrays as efficient catalyzer for high-performance lithium/sulfur batteries. *Nano Energy* **2021**, *84*, 105891.

[30] Xie, J.; Li, B. Q.; Peng, H. J.; Song, Y. W.; Zhao, M.; Chen, X.; Zhang, Q.; Huang, J. Q. Implanting atomic cobalt within mesoporous carbon toward highly stable lithium-sulfur batteries. *Adv. Mater.* **2019**, *31*, 1903813.

[31] Hao, G. P.; Tang, C.; Zhang, E.; Zhai, P. Y.; Yin, J.; Zhu, W. C.; Zhang, Q.; Kaskel, S. Thermal exfoliation of layered metal-organic frameworks into ultrahydrophilic graphene stacks and their applications in Li-S batteries. *Adv. Mater.* **2017**, *29*, 1702829.

[32] Sun, D.; Zhou, J. B.; Rao, D. W.; Zhu, L. Q.; Niu, S. W.; Cai, J. Y.; Fang, Y. Y.; Liu, Y.; Liu, X. M.; Zang, Y. P. et al. Regulating the electron filling state of d orbitals in Ta-based compounds for tunable lithium-sulfur chemistry. *Sustain. Mater. Technol.* **2021**, *28*, e00271.

[33] Li, Z. H.; Zhou, C.; Hua, J. H.; Hong, X. F.; Sun, C. L.; Li, H. W.; Xu, X.; Mai, L. Q. Engineering oxygen vacancies in a polysulfide-blocking layer with enhanced catalytic ability. *Adv. Mater.* **2020**, *32*, 1907444.

[34] Jin, Z. S.; Lin, T. N.; Jia, H. F.; Liu, B. Q.; Zhang, Q.; Li, L.; Zhang, L. Y.; Su, Z. M.; Wang, C. G. Expediting the conversion of Li_2S_2 to Li_2S enables high-performance Li-S batteries. *ACS Nano* **2021**, *15*, 7318–7327.

[35] Lei, T. Y.; Chen, W.; Lv, W. Q.; Huang, J. W.; Zhu, J.; Chu, J. W.; Yan, C. Y.; Yan, Y. C.; He, W. D.; Xiong, J. et al. Inhibiting polysulfide shuttling with a graphene composite separator for highly robust lithium-sulfur batteries. *Joule* **2018**, *2*, 2091–2104.

[36] Li, Z. Q.; Li, C. X.; Ge, X. L.; Ma, J. Y.; Zhang, Z. W.; Li, Q.; Wang, C. X.; Yin, L. W. Reduced graphene oxide wrapped MOFs-derived cobalt-doped porous carbon polyhedrons as sulfur immobilizers as cathodes for high performance lithium sulfur batteries. *Nano Energy* **2016**, *23*, 15–26.

[37] Jin, Z. S. ; Lin, T. N. ; Jia, H. F. ; Liu, B. Q. ; Zhang, Q. ; Chen, L. H. ; Zhang, L. Y. ; Li, L. ; Su, Z. M. ; Wang, C. G. *In situ* engineered ultrafine NiS_2-ZnS heterostructures in micro-mesoporous carbon spheres accelerating polysulfide redox kinetics for high-performance lithium-sulfur batteries. *Nanoscale* **2020**, *12*, 16201–16207.

[38] Jin, Z. S.; Liang, Z. M.; Zhao, M.; Zhang, Q.; Liu, B. Q.; Zhang, Q. Y.; Chen, L. H.; Li, L.; Wang, C. G. Rational design of MoNi sulfide yolk–shell heterostructure nanospheres as the efficient sulfur hosts for high-performance lithium-sulfur batteries. *Chem. Eng. J.* **2020**, *394*, 124983.